

# NUMERICAL WAVE TANKS BASED ON FINITE ELEMENT AND BOUNDARY ELEMENT MODELLING

## **R. Eatock Taylor<sup>1</sup>**

Department of Engineering Science

University of Oxford

Parks Road, Oxford OX1 3PJ, UK

e-mail: r.eatocktaylor@eng.ox.ac.uk

## **G. X. Wu**

Department of Mechanical Engineering

University College London

Torrington Place, London WC1E 7JE, UK

## **W. Bai**

Department of Engineering Science

University of Oxford

Parks Road, Oxford OX1 3PJ, UK

## **Z. Z. Hu**

Department of Mechanical Engineering

University College London

Torrington Place, London WC1E 7JE, UK

## **ABSTRACT**

This work forms part of an investigation into the non-linear interaction between steep (but not overturning) transient waves and flared structures, using a coupled finite element and boundary element model. The use of a coupled approach is based on consideration of the relative strengths and weaknesses of the finite element (FE) and boundary element (BE) methods when implemented separately (e.g. efficiency of computation versus complexity of adaptive mesh generation).

---

<sup>1</sup> Corresponding Author

Based on a paper presented at 24<sup>th</sup> International Conference on Offshore Mechanics and Arctic Engineering (OMAE2005), June 12-16, 2005, Halkidiki, Greece

An FE model can be used to advantage away from the body, where the domain is regular, and a BE discretisation near the body where the moving mesh is complex.

The paper describes aspects of the FE and BE models which have been developed for this analysis, each based on the use of quadratic isoparametric elements implemented in a mixed Eulerian-Lagrangian formulation. Initially the two approaches have been developed side by side, in order to ensure the use of robust components in the coupled formulation. Results from these methods are obtained for a series of test cases, including the interaction of an impulse wave with a circular cylinder in a circular tank, and non-linear diffraction by a cylinder in a long tank.

Keywords: Numerical wave tank, boundary element, finite element, non-linear diffraction

## **INTRODUCTION**

The development of numerical wave tanks is following a number of directions, linked to different mathematical models (potential and viscous flows) and different techniques for discretisation. Reviews have been given by Kim et al [1] and Tanizawa [2]. Some of this work is motivated by investigations of wave breaking processes (initially in the absence of bodies), where rotational effects must be modelled; while other studies are focussed on non-linear diffraction processes where the assumptions of potential flow are still appropriate. The present paper falls within the second of these categories, and the waves are assumed to be non-overturning. The aim of representing the fully non-linear transient flow past complex underwater geometries has motivated the developments of models discretised by unstructured grids. Prominent amongst these are boundary element (BE) and finite element (FE) models. Examples of the BE approach are papers by Celebi et al [3], Liu et al [4] and Ferrant et al [5].

In a direct comparison between BE and FE models of the non-linear wave-body interaction problem, Wu & Eatock Taylor [6] showed that the FE approach had significant advantages. Despite the need to discretise the whole flow domain in the FE approach, but only the boundary when the BE method is used, the computational resources required to handle the fully populated BE matrices were found to be very substantially larger. As a result, a series of investigations followed which were based on FE models [7-13]. During the course of this work, a feasibility study of a coupled FE-BE approach was also conducted [14], in 2D. The present work is directed towards extending this coupled approach to 3D. A potential drawback of the FE method is the complexity of generating the mesh around, say, a flared body, following the body

motions and the deformation of the free surface with the passage of waves. The idea of the coupled approach is to use the BE method in a small domain around the body (with limited memory requirement for the associated full matrices); and to use a simple FE model in the large outer domain, where a simple structured mesh may be used in conjunction with sparse matrix storage and solution routines (see figure 1). To achieve this, it is necessary to ensure suitable continuity between the outer (FE) and inner (BE) domains at each time step, which in [14] is achieved through an iteration based on the Domain Decomposition method. In a 3D coupled model using Domain Decomposition, continuity between adjacent domains is through the nodes on vertical boundary surfaces. It is appropriate to use similar levels of approximation in both domains, and here both the FE and the BE models employ quadratic isoparametric elements.

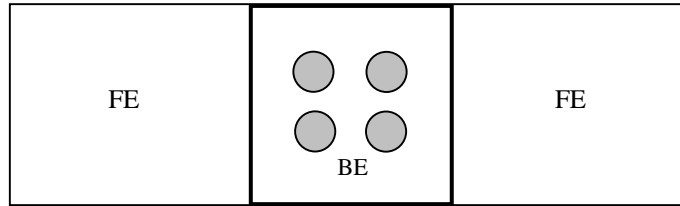


**Fig. 1 Coupled BE/FE mesh regions on free surface for four cylinders in a wave tank**

These 3D BE and FE fully non-linear models are first being developed and verified independently, prior to incorporation in the coupling algorithms. Each is implemented in a mixed Eulerian-Lagrangian formulation. This paper describes the particular features of the approach adopted, and provides illustrative results and comparisons with other data by way of verification.

## OVERALL FORMULATION

The problem is formulated in terms of a velocity potential  $\phi(x, y, z, t)$ , in a Cartesian system of axes  $Oxyz$  having the origin  $O$  on the mean free surface and  $z$  pointing upwards. The potential satisfies Laplace's equation, and conditions on the free surface,  $S_f$ , which in a Lagrangian description can be written (e. g. Longuet-Higgins and Cokelet [15])

$$\frac{Dx}{Dt} = \nabla \phi, \quad (1)$$

$$\frac{D\phi}{Dt} = -gz + \frac{1}{2} \nabla \phi \cdot \nabla \phi, \quad (2)$$

with  $\mathbf{x} = \{x \ y \ z\}$  and  $g$  being the acceleration due to gravity. In this paper we take the body to be fixed, so the boundary condition on the body surface  $S_B$  has the same form as that on the tank walls,  $S_W$ , and on the horizontal bottom of the tank,  $S_G$ , namely the Neumann condition:

$$\frac{\partial \phi}{\partial n} = 0, \quad (3)$$

where  $\mathbf{n}$  is the normal vector pointing out of the fluid domain. The condition on the piston wavemaker,  $S_M$ , is

$$\frac{\partial \phi}{\partial n} = \mathbf{U}_0 \cdot \mathbf{n}, \quad (4)$$

where  $\mathbf{U}_0$  is its velocity. The radiation condition at the downstream end of the tank is imposed using a damping layer on the free surface. In the FE model this is coupled with a modified Sommerfeld condition on a vertical plane [10].

Both the BE and FE procedures solve for nodal values of  $\phi$  at each time step, subject to the boundary conditions given in Eq. (3) and (4), the radiation condition, and a Dirichlet condition on the current free surface configuration. At the first time step this can be taken as  $\phi = 0$  on  $S_F$ , and subsequently  $\phi = \phi_F$  is obtained through numerical integration of Eq. (2) using values from previous time steps (e.g. with Runge Kutta or Adams-Bashforth algorithms). The new positions of free surface nodes are similarly obtained by numerical integration of Eq. (1).

To achieve the new values of  $\phi$  and  $\mathbf{x}$  on the free surface, it is necessary first to evaluate the velocities. Several methods have been investigated, as described in the cited references. Here we have used a straightforward approach expressing the velocities in terms of the derivatives of the element shape functions (which are assumed to be quadratic in both the BE and FE domains). Details are given in the following sections covering the BE and FE representations respectively.

The hydrodynamic forces on the body are expressible as

$$\mathbf{F} = -\rho \iint_{S_B} (\phi_t + \frac{1}{2} \nabla \phi \cdot \nabla \phi + gz) \mathbf{n} \, ds \quad (5)$$

with a corresponding expression for the moments. The velocity components  $\nabla \phi$  on the body surface may be obtained using the approach discussed below for deriving the free surface velocities in the BE approach (using the known normal velocity, and tangential velocities obtained via the derivatives of the shape functions). More difficult, however, is the

evaluation of  $\phi_t$  in Eq. (5). Estimating this quantity using backwards differences is inaccurate and prone to instabilities (particularly in the more general case when the body is free to move). Another approach for a fixed body, used in [10, 11], is to solve a separate boundary value problem for  $\phi_t$ , which also satisfies Laplace's equation, and corresponding boundary conditions on the body, the bottom and sidewalls, and the wavemaker, as well as the same radiation condition as  $\phi$ . On the free surface we have

$$\phi_t = -gz - \frac{1}{2} \nabla \phi \cdot \nabla \phi. \quad (6)$$

The solution for  $\phi_t$  on the body surface may then be obtained from the solution of this second problem at each time step.

Since the free surface nodes move, it becomes necessary to regenerate the governing BE and FE matrices. This need not be done at every time step. But when remeshing is performed, information corresponding to the new positions of the nodes must be obtained by interpolation of data pertaining to the old positions. First one must establish in which old element each new node is located. The interpolations may then be conveniently undertaken by projection of the free surface BE elements, or the free surface faces of the 3D FE elements, onto a horizontal plane, and use of the 2D quadratic element shape functions. Further details are given below.

## THE BOUNDARY ELEMENT MODEL

**Higher-order BE method** The boundary element method is widely used to solve the mixed boundary value problem in the numerical simulation of wave tanks, because it can reduce the dimension of the problems to be solved by one. If a Rankine source is used as the Green's function,  $G$ , a boundary integral equation for the potential  $\phi$  over the whole boundary  $S$  can be derived, expressing the original potential flow problem through Green's second identity:

$$C(\mathbf{x}_0)\phi(\mathbf{x}_0) = \iint_S \left[ G(\mathbf{x}, \mathbf{x}_0) \frac{\partial \phi(\mathbf{x})}{\partial n} - \phi(\mathbf{x}) \frac{\partial G(\mathbf{x}, \mathbf{x}_0)}{\partial n} \right] dS. \quad (7)$$

Here  $C(\mathbf{x}_0)$  is the solid angle at the field point  $\mathbf{x}_0$ , and  $\mathbf{n}$  is measured from the source point  $\mathbf{x}$ . For cases in which the body and the simulated flow are symmetric about the  $x$ - $z$  plane, and the seabed is horizontal (as considered here), the simple Rankine source and its image with respect to the symmetry plane ( $y = 0$ ) and the seabed ( $z = -d$ ) can be chosen as the

Green's function. Thus, the integral need only be evaluated over the body surface  $S_B$ , the free surface  $S_F$ , the wavemaker  $S_M$  and the tank walls  $S_W$ <sup>2</sup>. Under this condition, the Green's function can be written as

$$G(\mathbf{x}, \mathbf{x}_0) = \frac{1}{4\pi} \left( \frac{1}{R_1} + \frac{1}{R_2} + \frac{1}{R_3} + \frac{1}{R_4} \right), \quad (8)$$

where

$$\begin{cases} R_1 = \sqrt{(x-x_0)^2 + (y-y_0)^2 + (z-z_0)^2} \\ R_2 = \sqrt{(x-x_0)^2 + (y+y_0)^2 + (z-z_0)^2} \\ R_3 = \sqrt{(x-x_0)^2 + (y-y_0)^2 + (z+z_0+2d)^2} \\ R_4 = \sqrt{(x-x_0)^2 + (y+y_0)^2 + (z+z_0+2d)^2} \end{cases}. \quad (9)$$

It is well known that the higher-order boundary element method is more efficient and accurate than the constant panel method. In the higher-order BE method, the surface over which the integral is written is discretised by  $N$  quadratic isoparametric elements. Eight and six nodes are placed on curved quadrilateral and triangular elements respectively. After introducing shape functions  $N_j(\xi, \eta)$  in each surface element, in an analogous manner to that used in the FE method, one can write the position coordinate, the velocity potential and its derivatives within an element in terms of nodal values, in the following forms:

$$\mathbf{x}(\xi, \eta) = \sum_{j=1}^K N_j(\xi, \eta) \mathbf{x}_j; \quad \phi(\xi, \eta) = \sum_{j=1}^K N_j(\xi, \eta) \phi_j; \quad (10)$$

$$\frac{\partial \phi(\xi, \eta)}{\partial \xi} = \sum_{j=1}^K \frac{\partial N_j(\xi, \eta)}{\partial \xi} \phi_j; \quad \frac{\partial \phi(\xi, \eta)}{\partial \eta} = \sum_{j=1}^K \frac{\partial N_j(\xi, \eta)}{\partial \eta} \phi_j, \quad (11)$$

where  $K$  is the number of nodes in the element,  $\mathbf{x}_j$  and  $\phi_j$  are the nodal positions and potentials, and  $(\xi, \eta)$  are local intrinsic coordinates. By substituting these representations into Eq. (7), the boundary integral equation in the discretised form can be rewritten as:

$$C(\mathbf{x}_0)\phi(\mathbf{x}_0) = \sum_{n=1}^N \sum_{m=1}^M \left\{ G(\mathbf{x}_m, \mathbf{x}_0) \left[ \sum_{j=1}^K N_j(\xi, \eta) \left( \frac{\partial \phi}{\partial n} \right)_j \right] - \frac{\partial G(\mathbf{x}_m, \mathbf{x}_0)}{\partial n} \left[ \sum_{j=1}^K N_j(\xi, \eta) \phi_j \right] \right\} w_m |J_m(\xi, \eta)| \quad (12)$$

<sup>2</sup> When the BE method is to be coupled with the FE method, the BE domain must also include vertical boundary surfaces adjacent to the FE domains at each end.

where  $M$  is the number of sampling points used in the standard Gauss-Legendre method to evaluate numerically the integration over each element,  $w_m$  is the integral weight at the  $m$ th sampling point, and  $J_m(\xi, \eta)$  is the Jacobian transformation from the global to the local intrinsic coordinates. When the field point is located within the element, the associated singularity is evaluated by using the triangular polar-coordinate transformation technique described by Eatock Taylor & Chau [16]. At a certain time step, either the potential or its normal derivative on each part of the boundary is known from the corresponding boundary conditions: the remaining unknowns can then be calculated by solving the above discretised equation.

We observe that the solid angle  $C(\mathbf{x}_0)$  still needs to be determined, and it is difficult to compute directly for the complex evolving three-dimensional computational domain. However, the treatment of the solid angle can be simplified by using the physical argument that a uniform potential applied over a closed domain produces no flux. This is equivalent to considering a homogeneous Dirichlet problem, in which a uniform field,  $\phi = \text{constant} \neq 0$ , is specified over the whole integral boundary  $S$ . The boundary integral equation, Eq. (7), in such a case leads to

$$C(\mathbf{x}_0) = - \iint_S \frac{\partial G(\mathbf{x}, \mathbf{x}_0)}{\partial n} dS. \quad (13)$$

This convenient formula expresses the solid angle as an integration of the derivative of the Green's function, which can be obtained directly from the influence coefficients without additional work.

The resulting matrix equation can finally be expressed in the matrix form:

$$[A]\{\Phi\} = \{B\}, \quad (14)$$

where

$$\{\Phi\} = \left[ \phi_1, \phi_2, \dots, \phi_{N_n}, \left( \frac{\partial \phi}{\partial n} \right)_1, \left( \frac{\partial \phi}{\partial n} \right)_2, \dots, \left( \frac{\partial \phi}{\partial n} \right)_{N_p} \right]^T; \quad (15a)$$

$$[A_{i,j}^{(1)}] = \delta \cdot C(\mathbf{x}_i) + \sum_{n=1}^{N_n} \sum_{m=1}^M \left[ \frac{\partial G(\mathbf{x}_m, \mathbf{x}_i)}{\partial n} N_j(\xi, \eta) w_m |J_m(\xi, \eta)| \right]; \quad (15b)$$

$$[A_{i,j}^{(2)}] = - \sum_{n=1}^{N_p} \sum_{m=1}^M [G(\mathbf{x}_m, \mathbf{x}_i) N_j(\xi, \eta) w_m |J_m(\xi, \eta)|]; \quad (15c)$$

$$\{B\} = -(1 - \delta) \cdot C(\mathbf{x}_i) \phi(\mathbf{x}_i) + \sum_{n=1}^{N_n} \sum_{m=1}^M \left[ G(\mathbf{x}_m, \mathbf{x}_i) \frac{\partial \phi(\mathbf{x}_m)}{\partial n} w_m |J_m(\xi, \eta)| \right] \sum_{n=1}^{N_p} \sum_{m=1}^M \left[ \frac{\partial G(\mathbf{x}_m, \mathbf{x}_i)}{\partial n} \phi(\mathbf{x}_m) w_m |J_m(\xi, \eta)| \right] \quad (15d)$$

We use  $S_n$  and  $S_p$  to denote the Neumann and Dirichlet boundaries respectively, and  $N_n$  and  $N_p$  are the numbers of elements on each of these;  $\delta$  equals 1 when the node  $\mathbf{x}_i$  is situated on  $S_n$ , otherwise it is zero.

Unstructured meshes are particularly suited to discretising complex domain boundaries. For the BE model, therefore, an unstructured triangular mesh is adopted on the free surface (which is also appropriate for the extension to the coupled BE/FE model), with simple structured quadrilateral meshes on the vertical surfaces bounding the BE domain.

**Artificial damping layer** A numerical beach is incorporated at the far end of the tank, by modifying the kinematic and dynamic conditions over a finite length of the free surface. The approach has been discussed elsewhere, e.g. in the 2D case by Clément [17]. We write:

$$\frac{D\mathbf{X}}{Dt} = \nabla \phi - \nu(x)(\mathbf{X} - \mathbf{X}_e), \quad (16)$$

$$\frac{D\phi}{Dt} = -gz + \frac{1}{2} \nabla \phi \cdot \nabla \phi - \nu(x)\phi, \quad (17)$$

where  $\nu(x)$  is the damping coefficient, and  $\mathbf{X}_e = (x_e, y_e, 0)$  is a reference value specifying the at-rest position of the fluid particle. In practice, the damping coefficient is chosen to be continuous and continuously differentiable, and is “tuned” to a characteristic frequency  $\omega$  of the incident wave. Here we have used:

$$\nu(x) = \begin{cases} \alpha \omega \left( \frac{x - x_0}{\beta \lambda} \right)^2 & x_0 \leq x \leq x_1 = x_0 + \beta \lambda \\ 0 & x < x_0 \end{cases} \quad (18)$$

In this definition,  $\lambda$  is the incident wavelength, and  $x_0$  is the coordinate of the point on the damping layer nearest to the wave maker; and the two non-dimensional parameters  $\alpha$  and  $\beta$  are used to control the strength of the damping and the length of the damping layer respectively. These are both chosen to be 1.0 for the results given here.

**Time stepping integration** The free surface geometry and potential are updated by integrating the free surface boundary conditions in time, in an iterative manner. Here, the standard 4th-order Runge-Kutta scheme (RK4) is used, providing good stability characteristics within a convenient computational scheme.

One first needs to compute the free surface particle velocities. Based on the known potential and its normal derivative on the boundary of the whole fluid domain, in conjunction with the higher-order BE method being adopted, the particle velocities both on the free and body surfaces can be easily determined by use of the following formula:

$$\begin{bmatrix} \frac{\partial \phi}{\partial x} \\ \frac{\partial \phi}{\partial y} \\ \frac{\partial \phi}{\partial z} \end{bmatrix} = \begin{bmatrix} \frac{\partial x}{\partial \xi} & \frac{\partial y}{\partial \xi} & \frac{\partial z}{\partial \xi} \\ \frac{\partial x}{\partial \eta} & \frac{\partial y}{\partial \eta} & \frac{\partial z}{\partial \eta} \\ n_x & n_y & n_z \end{bmatrix}^{-1} \begin{bmatrix} \frac{\partial \phi}{\partial \xi} \\ \frac{\partial \phi}{\partial \eta} \\ \frac{\partial \phi}{\partial n} \end{bmatrix}. \quad (19)$$

**Intersection line** The intersections between the free water surface and the solid boundaries such as the wave maker, tank walls and a fixed or floating body, define sharp edges and corners on the domain boundary. As a higher-order BE method is adopted, the field point  $\mathbf{x}_0$  can be located at the corner or edge of the boundary surface, and this will result in a singularity where the normal vector at the point is undefined. To deal with such a singularity, a double or triple node technique is employed in the simulation at the edges or corners. This places two or three different nodes at one spatial position to represent the different normal vectors. It should be noticed that on the intersection of the free surface and the body surface, the potential on the free surface is known from the free surface boundary condition, and therefore the potential on the body surface is also known, according to the continuity of potential. There are no unknown variables for the double or triple nodes on the body surface, and the corresponding terms are moved to the right-hand side of the equation.

At each time step, the time integration of the free surface boundary conditions can give the new positions of the double or triple nodes on the free surface. However, it is found from the numerical experiments that these nodes can separate from the body surface due to numerical error (though the separation is always very small). In order to determine the intersection, we simply force the double or triple nodes on the free surface back onto the body surface along the normal direction of the body surface.

**Algebraic equation solver** The solution of the full and unsymmetric influence matrix arising from the mixed boundary value problem is a significant part of the calculation. A direct solution of the linear equations would require an effort of  $O(N^3)$ . Here, the generalized minimum residual (GMRES) iterative scheme with a diagonal preconditioner is used, and found to be very efficient.

**Saw-tooth instability** Under most conditions, the numerically computed wave profile will, after a sufficiently long time, develop a saw-tooth appearance. This problem was identified and discussed by Longuet-Higgins and Cokelet [15]. The regriding technique implemented here in the BE model removes this numerical instability. This avoids the arbitrariness of having to choose an explicit smoothing formula. To realize the mesh regeneration on the free surface, interpolation is used to predict the vertical coordinate of the new node based on the given horizontal coordinate. For boundary-fixed problems, the horizontal coordinate is computed at the initial time step, and then can be used at the following time steps. However, for many moving boundary problems, such as wave making or floating body cases, we need to move the nodes horizontally prior to the vertical interpolation, in order to maintain a uniform distribution of nodes and good aspect ratios for the elements. This is achieved by starting from the new position of nodes obtained from the time stepping integration and using a method such as the Laplacian smoothing technique, *i.e.*:

$$(x, y)_i = \frac{1}{P} \sum_{j=1}^P (x, y)_j, \quad (20)$$

where  $P$  is the total number of nodes located around the node  $i$ .

In the interpolation, one must first find which old free surface element each new node belongs to, because when the fluid domain is remeshed, the new node cannot automatically be attached to a particular old element. To find the corresponding old element, the following criterion is used:

$$\sum_{k=1}^Q S_{sub}^k = S_{ele}, \quad (21)$$

where  $Q$  is the number of triangular sub-elements,  $S_{sub}$  is the area of the triangular sub-element that consists of two vertices of the old element and the considered node, and  $S_{ele}$  is the area of the old element. If the equation is satisfied, the node must lie inside this element. The following numerical integration is used to calculate the area of a triangular element:

$$S = \sum_{m=1}^M w_m |J_m(\xi, \eta)|. \quad (22)$$

Finally the local intrinsic coordinates  $(\xi, \eta)$  can be determined based on the areas of sub-elements and the old element, and the vertical coordinate and potential at the node can subsequently be obtained by using the shape function within this old element.

## THE FINITE ELEMENT MODEL

The approach described in [7-11 and 13] used 4-noded tetrahedral elements with linear shape functions. Here we use 15-noded prism elements with quadratic shape functions. These have advantages for the development of the coupled BE-FE method. The isoparametric model may again be represented along the lines of Eq. (10) and Eq. (11), though now the potential and coordinates are functions of the three intrinsic coordinates  $(\xi, \eta, \zeta)$  within the volume element. The FE equations are obtained by employing the Galerkin method, namely by using:

$$\iiint_{\forall} \nabla^2 \phi N_i dV = 0, \quad (23)$$

within the FE domain  $\forall$ .

Through use of Green's identity and the boundary conditions, this equation is transformed into

$$\iiint_{\forall} \nabla N_I \cdot \sum_{J \notin S_p} \phi_J \nabla N_J dV = \iint_{S_n} N_I f_n dS - \iiint_{\forall} \nabla N_I \cdot \sum_{J \in S_p} (f_p)_J \nabla N_J dV \quad (I \notin S_p) \quad (24)$$

Here, as above,  $S_p$  represents the Dirichlet boundary on which the velocity potential, denoted now by  $f_p$ , is known, and  $S_n$  represents the Neumann boundary on which the normal derivative of the velocity potential, denoted by  $f_n$ , is known. The equation can further be written in the matrix form:

$$[A]\{\Phi\} = \{B\}, \quad (25)$$

where

$$\{\Phi\} = [\phi_1, \phi_2, \phi_3, \dots, \phi_I, \dots]^T \quad (I \notin S_p) \quad (26)$$

$$A_{IJ} = \iiint_{\forall} \nabla N_I \cdot \nabla N_J d\forall \quad (I \notin S_p \text{ and } J \notin S_p) \quad (27)$$

$$B_{I1} = \iint_{S_n} N_I f_n dS, \quad (I \in S_n) \quad (28a)$$

$$B_{I2} = -\iiint_{\forall} \nabla N_I \cdot \sum_{J \in S_p} (f_p)_J \nabla N_J d\forall, \quad (I \notin S_p). \quad (28b)$$

The volume integrals in the prism elements in Eqs. (27) and (28b), are effected by integration over triangular and quadrilateral domains corresponding to the two triangular and three quadrilateral faces. These, and the surface elements

over quadrilaterals in Eq. (28a), are obtained by Gaussian quadrature. It has been found that 3x3 quadrature over quadrilaterals and 7 point quadrature over triangles leads to acceptable accuracy.

**Other features** Many of the other aspects of the FE implementation have similar features to what has been described above for the BE model. Further details are given in [13]. Wang and Wu [18] describe the method for dealing with saw-tooth instabilities which can arise in FE models used to simulate nonlinear water waves. A few further points are briefly highlighted here.

The radiation condition is implemented through a combination of a damping zone and the Sommerfeld condition [10], applied at nodes on the vertical plane at the end of the tank. The effective phase velocity  $c$  in this condition is specified through

$$\frac{c}{\sqrt{gd}} = \sqrt{\frac{\tanh kd}{kd}},$$

where  $k$  is an appropriate wave number. This is found to work well in the cases examined with non-linear periodic waves (obtaining  $k$  from the linear dispersion equation corresponding to the fundamental wave frequency). Care must be taken in establishing the position of the boundary on which this condition is applied (bearing in mind possible motion of the nodes); and in matching the behaviour of the potential on the vertical boundary at the far end with that on the free surface. These issues are discussed in detail in [10].

Unlike the matrix equations developed here for the BE model, those for the FE formulation are symmetric. (It would of course be possible to implement a Galerkin approach in the BE analysis, but that has not been done here). Furthermore, as mentioned above, the FE equations are sparse. Here a conjugate gradient iterative procedure with a Symmetric Successive Over-Relaxation preconditioner has been found to be very effective.

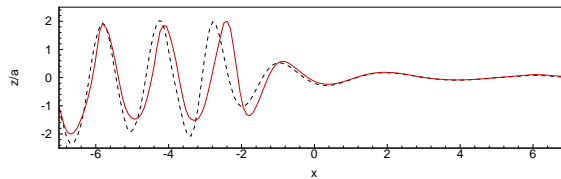
## RESULTS

In this section, three different numerical examples are investigated to validate the finite element and boundary element models. The water depth  $d$ , gravitational acceleration  $g$  and fluid density  $\rho$  are taken to be unity in all cases discussed below in order to show the results in non-dimensional form.

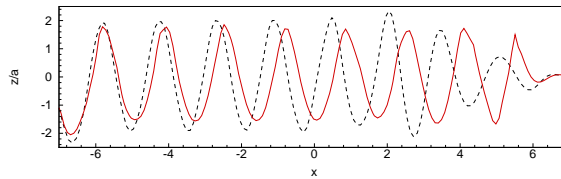
Firstly, wave propagation in a rectangular tank without any bodies is simulated with the BE model. The origin is situated at the centre of the rectangular wave tank, the total tank length of which is 14. Only half of the wave tank is considered due to symmetry, the half-width being taken as 0.62. At the left end of the wave tank, a monochromatic wave is generated by a piston-like wave-maker undergoing the following motion at frequency  $\omega$ :

$$\begin{cases} S_0(t) = -a \cos(\omega t) \\ U_0(t) = a\omega \sin(\omega t) \end{cases}, \quad (29)$$

where  $S_0(t)$  and  $U_0(t)$  are the displacement and velocity of the wave-maker respectively, and  $a$  is the amplitude of wave-maker motion. Near the right end of the wave tank, the damping zone is situated: this starts at a distance of one incident wavelength measured from the far end of the tank.



(a)



(b)

**Fig. 2 Spatial profile of propagating wave at  $\omega = 2.0$ :  $a=0.01$ (-----);  $a=0.043$  (——). a)  $t=7T$ ; b)  $t=15T$**

Figure 2 gives the spatial profiles of propagating waves at the incident wave frequency  $\omega = 2.0$ , for two different amplitudes. The number of triangular boundary elements used on the free surface is 672, and in total 1176 elements are generated on the domain boundaries. The duration of the calculation is  $15T$ , where  $T$  is the incident wave period, and the time interval  $\Delta t$  is chosen as  $0.05T$ . In order to avoid an abrupt initial condition, a cosine-type ramp function is used to modulate the wave-maker boundary condition, and the ramp time is equal to one incident wave period  $T$ . For these two cases, the amplitudes of the wave-maker motion are set to be 0.01 and 0.043 respectively, which correspond to the resulting waves having steepnesses  $\varepsilon = H/\lambda \approx 0.025$  and 0.085, where  $H$  is the wave height. It should be noted that for the smaller incident amplitude,  $a=0.01$ , the computation can run stably without mesh regeneration, due to the weak non-

linearity of the propagating wave. With the increase of amplitude to  $a=0.043$ , saw-tooth instability occurs. Remeshing is therefore applied every two time steps, which avoids overly distorted meshes. The results of Figure 2 suggest that this process does not lead to significant numerical dissipation in this case.

It can be seen from Figure 2(a) that at  $t=7T$  the steady state wave has not yet reached the damping zone, whereas in Figure 2(b) at  $t=15T$  it has occupied the whole wave tank. Figure 2(b) confirms that the artificial damping layer adopted on the free surface can absorb the wave energy efficiently, and no reflected waves can be seen disturbing the upstream wave field. We can also observe the expected non-linear behaviour, namely that the waves generated with the larger amplitude of the wave-maker motion have flatter troughs and sharper crests, and the wave profile and its amplitude are asymmetric about the mean position  $z=0$ . Moreover, the wave with larger amplitude travels faster and has longer wavelength than that with smaller amplitude. These wave conditions are used as input to the diffraction problem considered subsequently.

The second numerical example is to investigate an asymmetric initial wave in a circular cylindrical tank with a surface-piercing cylinder at its centre. This case was studied by Chern *et al.* [19], using a pseudo-spectral matrix element method (PSME) to discretise the fully non-linear free surface problem. This problem tests the ability of the present BE model to simulate the complex non-linear diffracted wave patterns around the inner cylinder, and the calculation of the resulting horizontal wave force. The formula for the initial wave profile is defined as:

$$z(t=0) = a \exp \left[ - \left( x - \frac{r_I + r_0}{2} \right)^2 - y^2 \right], \quad (30)$$

where  $r_I$  and  $r_0$  are the radius of the inner cylinder and the outer cylindrical wall, (taken here taken as 1 and 10 respectively), and  $a$  is the amplitude of the initial wave profile, taken as 0.1. The peak of the impulse wave is located half way along the radial line between the walls of the inner and outer cylinders. The computational domain contains 1048 elements, and the non-dimensional time step is 0.1. Mesh regeneration is not needed in this case.

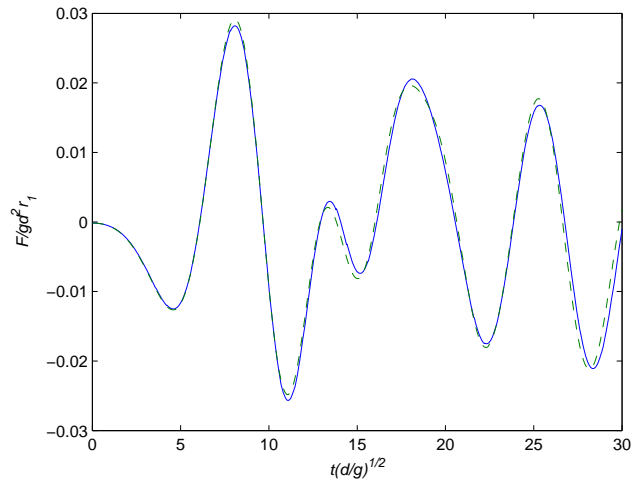


**Fig. 3 Time history of horizontal force on cylinder (—PSME; ---- BE)**

Figure 3 shows the time history of horizontal force acting on the inner cylinder and the comparison with the results of Chern *et al.* [19]. In this case, the combination of incident, reflected and diffracted waves leads to a rather complex force process. It can be seen that the two numerical results are in good agreement. In Figure 4, the comparison of free surface contours with those in Ref. [19] is shown at two dimensionless time instants,  $t = 15$  and  $30$  respectively. We can see that the agreement is basically satisfactory. However, in front of the inner cylinder some differences can be noted when the free surface elevation is small, because the asymmetric unstructured meshes on the free surface we used are much coarser than the discretisation in Ref. [19]. Figure 5 compares the time history of free surface elevation at the front of the inner cylinder. Again the results from the two methods agree well, apart from around  $16 < t < 21$ . It should be noted that the time step used for our BE analysis is much larger than that used in the PSME analysis of Ref. [19].

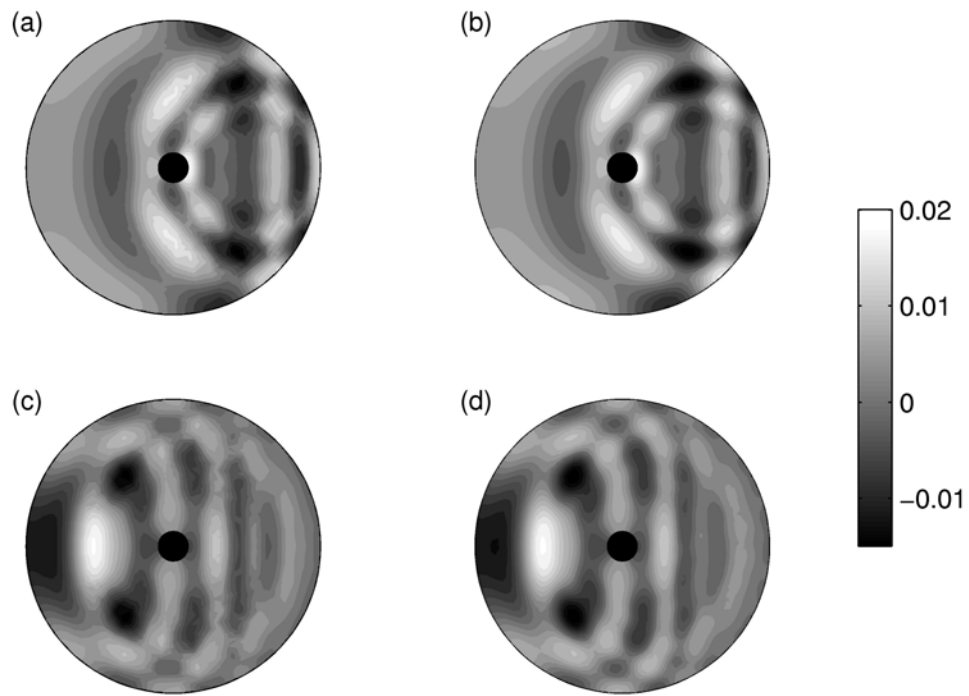


**Fig. 4 Free surface contours around cylinder at centre of circular tank,  $a = 0.1$ : a) PSME  $t=15$ ; BE  $t=15$ ; c) PSME  $t=30$ ; d) BE  $t=30$**

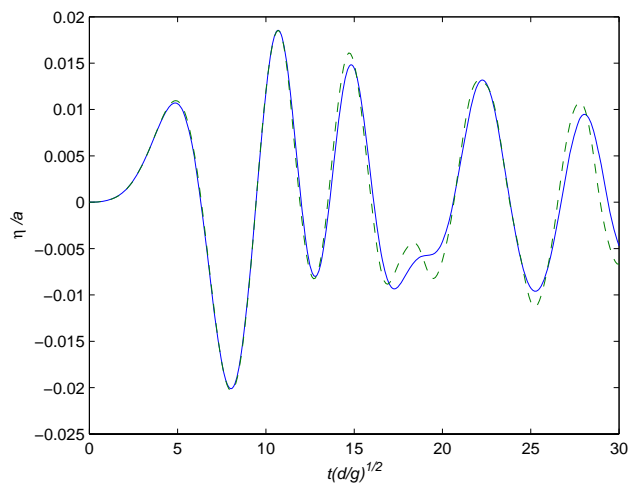


**Fig. 5 Time history of elevation at front of cylinder ( — PSME; ---- BE)**

Lastly, wave diffraction around a fixed vertical cylinder in a rectangular wave tank is calculated by using the linear and quadratic FE models, and the quadratic BE model. The wave tank and the BE meshes are similar to that used in the simulation of propagating waves discussed above, except that the half-width of the tank is now taken as 0.31. A fixed vertical circular cylinder of radius 0.1416 is situated at the centre of the tank. The meshes around the cylinder adopted in the BE and FE simulations are shown in Figure 6 (one plane of symmetry being shown in the former case). From this figure, it can be seen that the unstructured mesh around the body used in the BE model is more flexible and arbitrary than the corresponding FE mesh. This has advantages for discretising more complex problems, such as the wave-excited motions of flared structures.

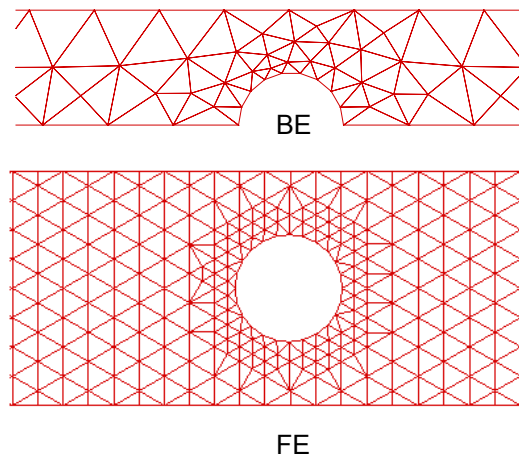


**Fig. 6 BE and FE meshes for cylinder in rectangular tank**

Figure 7 gives the time history of the force acting on the cylinder in the x-direction as obtained by the different numerical models, for the case of waves generated at frequency  $\omega = 2.0$  with the amplitude of the wave-maker motion being set at  $a = 0.01$ . An initial ramp function is not adopted in the BE simulation, in order to keep the case exactly the same as that calculated by the FE simulations.

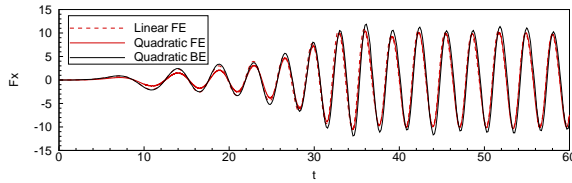


**Fig. 7 Time history of force on fixed cylinder in rectangular tank.**

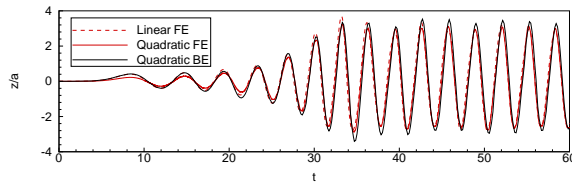


**Fig. 8 Time history of up-wave run-up**

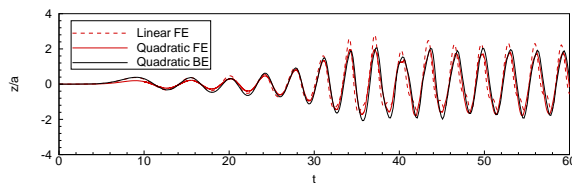


**Fig. 9 Time history of down-wave run-up**

The corresponding results for run-up at the extreme up-wave and down-wave points at the intersection of the cylinder and the free surface are shown in Figures 8 and 9 respectively. It can be seen from these three figures that the comparisons of wave force and wave run-up indicate good agreement between the different simulations, providing support for the accuracy of the linear and quadratic finite element models, and the quadratic boundary element model. As in the case of the propagating waves without bodies, there is no evidence of significant numerical dissipation in the solvers, and the numerical beaches/damping zones appear to be effective under the conditions we have considered.

## CONCLUDING REMARKS

Both boundary element and finite element methods have been developed to model the interaction of non-linear waves with bodies in a wave tank. Each is based on using quadratic isoparametric elements to implement an Euler-Lagrange formulation of the governing equations. The BE analysis is suited to modelling the domain around complex structures where the moving free surface, and in some cases body motions, require a highly efficient remeshing capability. The FE

approach however, as developed here, has particular advantages in the formulation and solution of the equations in circumstances where structured meshes may be employed (and the resulting coefficient matrices are sparse). It is believed that by coupling the two approaches (BE near the body and FE in the far field) an optimum numerical wave tank may be achieved. Because the BE and FE models described here share many similar features, in particular the quadratic variation over elements, such a coupling may be readily achieved as a further stage in this development. In principle the method can then be extended to the case of directional waves in a wide tank, subject to limitations on computational resources.

## **ACKNOWLEDGMENTS**

This work was supported by the Engineering and Physical Sciences Research Council through grants GR/S56917 at Oxford University and GR/S56900 at University College London.

## **REFERENCES**

- [1] Kim, C.H., Clement, A.H. and Tanizawa, K., 1999, "Recent Research and Development of numerical Wave Tanks - a Review", *Int. J. Offshore and Polar Engineering*, 9, pp. 241-256.
  
- [2] Tanizawa, K. 2000, "The State Of The Art On Numerical Wave Tank", *Proceeding of 4th Osaka Colloquium on Seakeeping Performance of Ships*, Osaka, Japan, 17-21 October, pp. 95-114.
  
- [3] Celebi, M.S., Kim, M.H. and Beck, R.F., 1998, "Fully Non-Linear 3D Wave Tank Simulation", *J. Ship Research*, 42, pp. 33-45.
  
- [4] Liu, Y. Xue, M. and Yue, D.K.P., 2001, "Computation of Fully Non-Linear Three-Dimensional Wave-Wave and Wave-Body Interactions, Part 2. Non-Linear Waves and Forces on a Body", *J. Fluid Mechanics*, 438, pp. 41-66.
  
- [5] Ferrant, P., Le Touzé, D. and Pelletier, K., 2003, "Non-Linear Time-Domain Models for Irregular Wave Diffraction about Offshore Structures", *Int. J. Numer. Meth. Fluids*, 43, pp. 1257-1277.
  
- [6] Wu, G.X. and Eatock Taylor, R., 1995, "Time Stepping Solutions of the Two Dimensional Non-Linear Wave Radiation Problem". *Ocean Engineering*, 22, pp. 785-798.

- [7] Wu, G.X. and Eatock Taylor, R., 1995, "Finite Element Analysis of Two Dimensional Non-Linear Transient Water Waves", *Applied Ocean Research*, 16, pp. 363-372.
- [8] Greaves, D.M., Borthwick, A.G.L., Wu, G.X. and Eatock Taylor, R., 1997, "A Moving Boundary Finite Element Method for Fully Non-Linear Wave Simulations", *J. Ship Research*, 41, pp. 181-194.
- [9] Wu, G.X., Ma, Q.W. and Eatock Taylor, R., 1998, "Numerical Simulation of Sloshing Waves in a 3D Tank Based on a Finite Element Method", *Applied Ocean Research*, 20, pp. 337-355.
- [10] Ma, Q.W., Wu, G.X. and Eatock Taylor, R., 2001, "Finite Element Simulation of Fully Non-Linear Interaction Between Vertical Cylinders and Steep Waves - Part 1: Methodology and Numerical Procedure", *Int. J. Numer. Meth. Fluids*, 36, pp. 265-285.
- [11] Ma, Q.W., Wu, G.X. and Eatock Taylor, R., 2001, "Finite Element Simulation of Fully Non-Linear Interaction between Vertical Cylinders and Steep Waves - Part 2: Numerical Results and Validation", *Int. J. Numer. Meth. Fluids*, 36, pp. 287-308.
- [12] Turnbull, M.S., Borthwick, A.G.L. and Eatock Taylor, R., 2003, "Numerical Wave Tank Based on a  $\eta$ -Transformed Finite Element Inviscid Solver", *Int. J. Numer. Meth. Fluids*, 6, pp. 641-663.
- [13] Wu, G.X. and Hu, Z.Z., 2004, "Simulation of Non-Linear Interactions between Waves and Floating Bodies through a Finite-Element-Based Numerical Tank", *Proceedings of the Royal Society, London*, A460, pp. 2797-2817.
- [14] Wu, G.X. and Eatock Taylor, R., 2003, "The Coupled Finite Element and Boundary Element Analysis of Non-Linear Interactions between Waves and Bodies", *Ocean Engineering*, 30, pp. 387-400.
- [15] Longuet-Higgins, M. S. and Cokelet, C. D., 1976, "The deformation of steep surface waves on water: I. A numerical method of computation", *Proc. R. Soc. Lond.*, A350, pp. 1-26.

[16] Eatock Taylor, R. and Chau, F. P., 1992, "Wave Diffraction Theory – some Developments in Linear and Non-Linear Theory", *J. Offshore Mechanics and Arctic Engineering*, 114, pp. 185-194.

[17] Clément, A., 1996, "Coupling of Two Absorbing Boundary Conditions for 2D Time-Domain Simulations of Free Surface Gravity Waves", *J. Comp. Phys.*, 126, pp. 139-151.

[18] Wang, C. Z. and Wu, G. X., 2006, "An unstructured-mesh-based finite element simulation of wave interactions with non-wall-sided bodies", *J. Fluids Struct.*, 22, pp. 441-461.

[19] Chern, M.J., Borthwick, A.G.L. and Eatock Taylor, R., 2001, "Simulation of Non-Linear Free Surface Motions in a Cylindrical Domain Using a Chebyshev-Fourier Spectral Collocation Method", *Int. J. Numer. Meth. Fluids*, 36, pp. 465-496.

## List of figures

Fig. 1 Coupled BE/FE mesh regions on free surface for four cylinders in a wave tank

Fig. 2 Spatial profile of propagating wave at  $\omega = 2.0$ :  $a = 0.01$  (·····);  $a = 0.043$  (——). a)  $t=7T$ ; b)  $t=15T$

Fig. 3 Time history of horizontal force on cylinder (——PSME; ---- BE)

Fig. 4 Free surface contours around cylinder at centre of circular tank,  $a = 0.1$ : a) PSME  $t = 15$ ; BE  $t = 15$ ; c) PSME  $t = 30$ ; d) BE  $t = 30$

Fig. 5 Time history of elevation at front of cylinder ( —— PSME; ---- BE)

Fig. 6 BE and FE meshes for cylinder in rectangular tank

Fig. 7 Time history of force on fixed cylinder in rectangular tank.

Fig. 8 Time history of up-wave run-up

Fig. 9 Time history of down-wave run-up